IRJMS

Numerical and Experimental Insights on Pitting Corrosion of Bare and Plasma Nitrided SS316L in Ground Granulated Blast-furnace Slag (GGBS) Concrete

Amol Mali[1]*, Aniket Kolekar[1], Vikas Dive[1], Sandesh Solepatil[1], Ganesh Jadhav[1], Sashikant Vagge[2]

[1]Department of Mechanical Engineering, D Y Patil International University, Akurdi, Pune, Maharashtra, India, [2]Department of Mechanical Engineering, Government College of Engineering, Jalgaon, Maharashtra, India. *Corresponding Author's Email: amol.mali@dypiu.ac.in

Abstract

Corrosion of concrete Rebar is persistently observed in building beams and columns. Due to this metallurgical problem, concrete structures become weak due to pitting corrosion of rebar, and the life of the building will be reduced. Products made of stainless steel are susceptible to corrosion in specific environments, mainly if they are open to a corrosive atmosphere, where localized oxidization may happen. This research examines how bare SS316L and plasma-nitrided SS316L respond to pitting corrosion in a Ground Granulated Blast-furnace Slag (GGBS) concrete environment. This research is unique because the chemical kinetics factors employed in the numerical model were established on an experimental campaign in Ground Granulated Blast-furnace Slag (GGBS) concrete environments. The primary emphasis of this work is pit development rather than the pitting start process. COMSOL Multiphysics simulation software is employed to complete 3D Finite element analysis (FEA) simulations in transient mode. Pits may be considered elliptical since, according to the examination of the investigational results, their mean width and depth are reasonably near together. In experimental results current density of bare (2.4×10^{-9} A/cm^2) and plasma nitrided SS316L (0.5×10^{-9} A/cm^2) stainless steel is observed. Experimental results of pitting corrosion are validated with Comsol multiphysics software for the current density of bare (2.12×10^{-9} A/cm^2) and plasma nitrided SS316L (0.33×10^{-9} A/cm^2) stainless steel is observed. According to numerical findings, the initial shape of the pit affects how it spreads. While an elliptical pit behaves differently, it maintains its form throughout propagation in radius over time.

Keywords: COMSOL Multiphysics, GGBS, Pitting Corrosion, Tafel plot.

Introduction

One of the primary types known as localized corrosion is pitting corrosion. On the exterior of the depassivated material, it causes microscopic holes that progressively get deeper. Therefore, most models now explain the pitting's propagation phase in a potential-static manner for localized pitting corrosion (1), using the finite element technique to create a 2D model. Finite element analysis (FEA) model describes the kinetics of anodic dissolution and suggests a critical i_{corr} for passivation that changes depending on the concentration of oxidization produced in the area. Depending on whether the solution is saturated (2), propose one-dimensional and two-dimensional FEA simulations with two dissolution establishments: the first regime regulated by Arrhenius-type initiation and the second by the diffusion of ionic species. A model of pitting evolution for fuel pipes in situations with high levels of sweet (CO_2) generation was created by suggested via the phase-field technique to mathematically represent the solid/liquid interface near the cavities in their novel numerical approach (3). The model can replicate the regions of the material's polarization curve connected to the various deterioration regimes (initiation, concentration, or mixed establishment). It has also been used to investigate the corrosion of composite materials and polycrystalline steels and the interaction between several pits. The spread of pitting on carbon steels or iron in a corrosive atmosphere has been numerically simulated as part of the study (3, 4). Consequently, 2D single-pit corrosion models that consider the precipitated phases may be used in

various environments with varying salinities and chemical compositions. Regarding pit geometry, corrosion current, and the impact of chloride ions, created pitting corrosion simulations that were realistic to Ni-based steel alloys (5). Modeling the pitting interactions caused by a stainless steel's chemical-mechanical stress, show that corrosion accelerates coalescence pitting (6). Additionally, their investigation demonstrated how the mechanical stress location affected pitting development. Pitting corrosion is a significant concern in strengthened concrete constructions, particularly in the instance of concrete rebars. This study uses experimental investigation and simulation techniques to investigate the pitting corrosion behavior of SS316L and plasma-nitrided SS316L rebars. The objective is to understand the effectiveness of ion nitriding as a surface modification method for enhancing the protection against corrosion of GGBS concrete rebars. Despite advancements in pitting corrosion research, several gaps remain. Limited studies explore plasma nitriding's effectiveness in GGBS concrete environments or its response under sweet (CO_2) corrosion conditions. The impact of pit geometry, particularly elliptical pits, on corrosion propagation is underrepresented, as is the role of GGBS in mitigating pitting. There is also a lack of integration between numerical simulations and experimental validation, especially for nitrided SS316L rebars. Additionally, long-term performance data and the interactions between multiple pits and mechanical stress in reinforced concrete structures are insufficiently studied. This research addresses these gaps to enhance corrosion resistance strategies for reinforced concrete. Pitting corrosion is one of the most destructive forms of localized corrosion, characterized by the formation of microscopic pits or cavities on the depassivated surface of materials, which can propagate over time. This phenomenon is particularly critical in reinforced concrete structures where corrosion can compromise structural integrity. The use of advanced surface modification techniques, such as plasma nitriding,

has shown promise in enhancing the corrosion resistance of stainless steel rebars. Ground Granulated Blast Furnace Slag (GGBS) concrete, known for its improved durability and reduced permeability, provides an ideal environment to study such effects. This research focuses on experimentally and numerically investigating the pitting corrosion behavior of bare SS316L and plasma-nitrided SS316L rebars in GGBS concrete. By leveraging COMSOL Multiphysics simulations and experimental methods, this study aims to provide insights into the mechanisms of corrosion resistance improvement through plasma nitriding and evaluate the impact of pit geometry on corrosion propagation. In summary, combining experimental analysis and simulation techniques using COMSOL Multiphysics software offers a comprehensive approach to investigating the pitting corrosion behavior of SS316L and plasma-nitrided SS316L rebars in GGBS concrete. The results provide valuable insights for the engineering and construction industry in developing corrosion-resistant reinforcement strategies to ensure reinforced concrete structures' long-term performance and safety. This work aims to use experimental and numerical simulation to investigate the behavior of bare 316L grade stainless steel and plasma nitrided 316L exposed to pitting corrosion in a GGBS concrete environment. The impact of a pit's form will also be covered by considering an elliptical pit.

Methodology

The material studied in this research was SS316L, commonly utilized for corrosion-resistant rebars. The initial condition of the material was in its as-received form, with a microhardness of 340 HV0.1. A lathe machine was employed to create the sample specimen, resulting in a rod shape with φ12 mm and a height of 500 mm. The SS316L underwent a 12-hour plasma nitriding heat treatment at 470 ℃ to improve its properties. Table 1 shows chemical composition of SS316L with the help of Spectroscopic Analysis.

Table 1: The Elemental Configuration of SS316 L

Elements	Fe	Cr	Mo	Ni	Si	Mn	C	S	P
W.t%	Balance	17	2.3	12	.03	2	.03	0.03	.04

Concrete Mix Design

This concrete mix design incorporates Ground Granulated Blast Furnace Slag (GGBS) as a partial replacement for cement, improving durability and sustainability. Table 2 provides the details of the concrete mix design, incorporating Ground Granulated Blast Furnace Slag (GGBS) as a partial replacement for cement. The binder consists of 70% cement (280 kg) and 30% GGBS (120 kg) for a total of 400 kg. Coarse aggregate is included at 1141 kg, ensuring strength and dimensional stability. A water-to-cementitious ratio of 0.35 is used, with 140 kg of water to achieve proper hydration and workability. This mix reduces the carbon footprint and is suitable for applications requiring enhanced durability, sulfate resistance, and reduced heat of hydration. It provides a balanced solution for both structural performance and environmental impact.

Table 2: Concrete Mix Design for GGBS Mixed Concrete

Cement %	GGBS %	Cement (kg)	GGBS (kg)	Coarse aggregate (kg)	Cement %	GGBS %	Cement (kg)
70%	30%	280	120	1141	803	0.35	140

Experimental Setup

In this experiment, a GGBS concrete column square specimen of size 50 mm x 50 mm x 500 mm was made of GGBS cement. The manufacturing process of a concrete building column involves several vital steps to ensure the production of a sturdy and durable structural element. It begins with carefully selecting and proportioning materials, including cement, sand, gravel, water, GGBS and any necessary additives or admixtures [7]. Once the mix design is established, the concrete is prepared by thoroughly blending the materials in a mixing machine, achieving a homogeneous and workable consistency. The freshly mixed GGBS concrete is then poured into the Concrete column square (prismatic column) of 50 mm x 50 mm x 500 mm, shaped to the required column dimensions, and compressed using an exciting bench to eliminate air voids.SS316L and plasma nitrided SS316L rebar is placed at the column's center after the initial curing period; the column is de-molded and transferred to a water-curing tank or chamber to maintain a moist environment, promoting proper hydration and strength development [8]. Figure 1 depicts a GGBS concrete column specimen that is prepared for corrosion test. After the prescribed curing duration, the column is subjected to various tests to assess its mechanical characteristics, such as compressive strength and stability. Once tested and approved, the GGBS concrete building column is ready to be used as a crucial load-bearing component in construction, ensuring the structural integrity and stability of the building.

Figure 1: A) GGBS Concrete Column Specimen with SS316L and **B)** Ground Granulated Blast-Furnace Slag (GGBS)
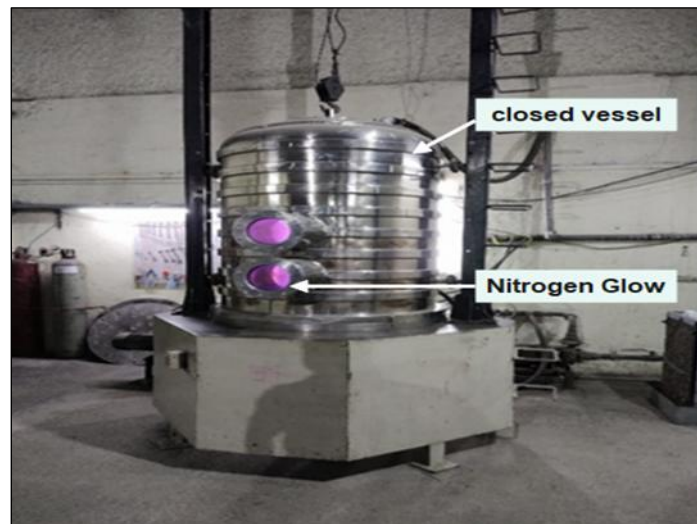
Surface Modification Technique - Plasma Nitriding

Plasma nitriding is a surface engineering method used to improve the characteristics of metal components. In this process, the material to be treated is placed in a vacuum chamber, and a gas mixture (usually nitrogen and hydrogen) is introduced into the cylindrical closed vessel [9]. Figure 2 depicts the plasma nitriding setup which is used for SS316L material processing. The gas is

then ionized to create plasma, which generates high-energy nitrogen ions. These nitrogen ions bombard the material's surface, causing nitrogen atoms to diffuse into the metal lattice. This affects hardened coatings of nitrides on the material's exterior. The depth and hardness of the nitrided layer can be estimated by modifying the method parameters such as temperature, pressure, and treatment time. This treatment was carried out at

450 °C for nitriding 12 hours. The process used a D.C. ion nitriding device with a gas combination of 50% N2 and 50% H2. The plasma nitriding setup used for the experiment is from "Shital Plasma Nitriding," located in Maharashtra, Bhosari, and Pune, India. Ion nitriding develops the Vickers hardness, wear resistance, and corrosion resistance of the material without significantly affecting its core properties.


Figure 2: Surface Modification Set Up: Plasma Nitriding Furnace

Corrosion Measurement Techniques

Corrosion experiments were carried out on IVIUM potentiostat/Galvanostat. Bare SS316L and plasma-nitrided SS316L were used as coupons for corrosion tests. A concrete mixture is used as an electrolyte (with 3.5 wt.% NaCl solution) having 2.5 S/m electrolyte conductivity. Using the IVIUM potentiostat, the Tafel tests were carried out on bare SS316L and 12 hr plasma nitrided SS316L materials. The three-electrode setup depicted in Figure 3 was employed to generate polarisation curves. The potential is supplied to the working electrode (WE), which in this example is a stainless steel bar, and its current reaction is seen. The platinum grid counter electrode dipped the square-shaped concrete samples into sodium chloride electrolyte (C.E.). The counter electrode (C.E.) delivers both current and potential to polarise the operational electrode. The reference electrode (RE) measures the operational electrode's instantaneous potential; RE is the third electrode. Saturated Calomel Electrode (SCE) was utilized in these tests. Before the

testing, the samples were immersed in water and fully saturated. During the Tafel tests and measurements of the corrosion potential, ϕ12 mm and 500 mm length of the piece was maintained out of the water (shown in Figures 3 and 4) not to limit the oxygen availability entirely. Electrochemical Impedance Spectroscopy (EIS) is based on the application of a low amplitude alternating current (AC) voltage signal usually 10-20 mV to the sample using a conventional three-electrode geometry electrochemical cell. In measuring the AC response of the system, the impedance is calculated at different frequencies. EIS data of sample is usually represented using bode plots, which display the logarithm of the impedance modulus [Z] and phase angle ø, versus the logarithm of frequency and or Nyquist plots which display impedance components in terms of the real impedance and imaginary impedance[IS 1727. (1967)](10).Plots is subsequently modeled using appropriate electrical circuits.
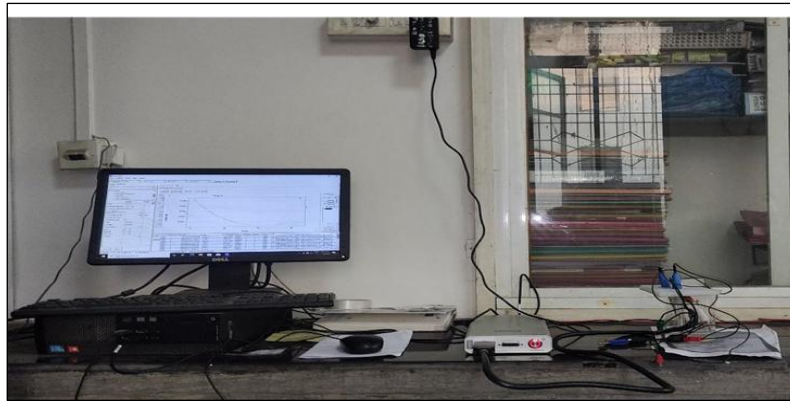
Figure 3: Experimental set up IVIUM Potentistat / Galvanostat

Pitting Corrosion Model Development

Two types of electrochemical corrosion cells, small pits leading to uniform/generalized corrosion, may coexist with chloride-instigated steel corrosion in GGBS concrete during the corrosion transmission stage (IS 12269. (1987)), (IS 383. (1970)); (IS 456. (2000)), including longitudinal pitting corrosion into the 3-D simulation model is necessary to improve the modeling of pitting corrosion in R.C. constructions. Figure 4 depicts a 2D view of a GGBS Concrete Column with an Elliptical Pit.

COMSOL Multiphysics® software was used to perform numerical simulations using a 2D axisymmetric model in transient mode (11). The mass conservation equation and the charge conservation equation are both solved numerically in this model. This led to the term "Corrosion, Tertiary with Electro neutrality interface" being used to characterize the movement of species (ions) in the electrolyte, the current distribution, and the pit's geometrical alterations.
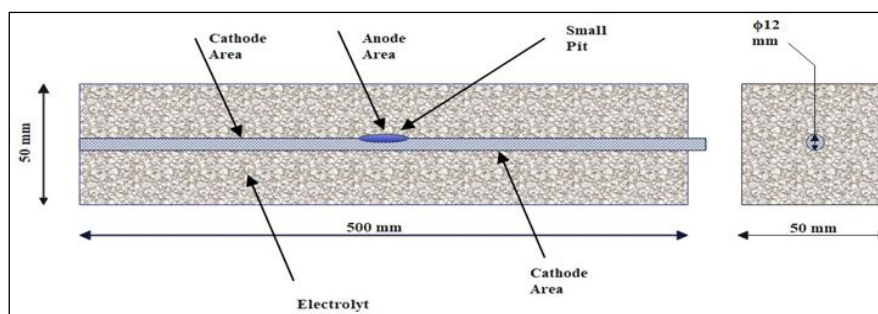
Figure 4: Experimental Setup of Concrete Column with Elliptical Pit

3D Geometric Modeling Simulation using COMSOL Multiphysics

In this investigation, the Laplace equation for the electric potential in the electrolyte [Eq.1], which changes over time due to the incoming flux from dissolution at the interface [Eq.2], was solved using the commercial software COMSOL multiphysics. Also, the current flux can be simplified as

$$i = -\frac{1}{\rho}\nabla E \qquad [1]$$

The current balance in the concrete electrolyte is given by

$$\nabla i = 0 \qquad [2]$$

The mesh you select for your COMSOL Multiphysics simulation significantly influences modeling needs. In reality, meshing is one of the memory-intensive phases when constructing and resolving a finite element problem. In current simulation model is mesh with the physics-controlled mesh of extra fine. Figure 5 shows the Three-dimensional geometry of Rebar inside GGBS concrete (electrolyte) in the column 50 x 50 x 500 mm. The outcome is a mesh with approximately 177837 elements with 60194 internal Degrees of freedom. The electrolyte conductivity of 2.5 S/m in the concrete column varies, with concrete providing a superior current resistance level. On concrete rebar of elliptical shape, 5 mm major axis, 2.5 minor axis, and depth of 20 mm were constructed on the reinforcement bar. These specifics are essential to the simulated experimental test.
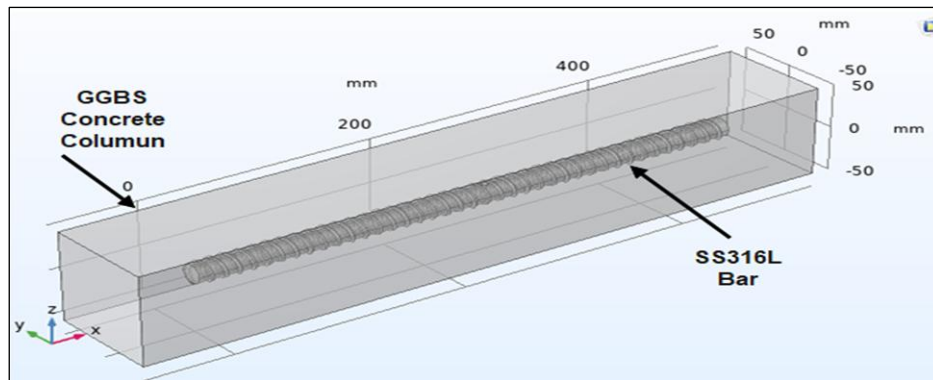
Figure 5: Three-dimensional Geometry of Rebar inside GGBS Concrete (electrolyte) the Column 50 x 50 x 500 mm

The use of 3D FEA and transient mode in COMSOL Multiphysics is essential for accurately modeling pitting corrosion, which involves complex pit geometries and time-dependent processes. A 3D approach captures realistic pit shapes, including irregular and elliptical pits, while transient mode simulates the dynamic evolution of pits and the localized electrochemical environment over time. This method effectively represents the diffusion of ions, chloride effects, and localized acidification. It also integrates mechanical stress effects, crucial for analyzing stress-induced pitting acceleration. Additionally, 3D transient simulations are well-suited to evaluate the time-dependent performance of plasma-nitrided surfaces in reinforced concrete, offering precise insights into corrosion mitigation strategies and long-term structural durability. The numerical model assumes uniform material properties and idealized environmental conditions, which may not fully reflect real scenarios. Approximations in boundary conditions and mesh resolution can impact accuracy, especially for complex pit geometries. Limited coupling of multiphysics processes and computational trade-offs in transient simulations may further reduce precision, while insufficient experimental validation can lead to discrepancies between simulations and actual behavior.

Results and Discussion

Microstructural Characterization

Microstructural and case depth characterization of SS316L was done by using an optical microscope as per ASTM E1077. The area with blue lines likely indicates the nitrided layer, showing the distinct boundary between the treated and untreated regions. The nitrided layer seems uniform, suggesting a well-controlled plasma nitriding process. Figure 6 depicts a microstructural view of the plasma nitriding depth of the CrN layer by Optical microscope. The case depth of the CrN layer is approximately 54 μm. The dark area on the right could be the base material, while the lighter region with the blue lines represents the nitrided layer. The microstructure visible in the image suggests that the nitriding process has successfully altered the surface properties of the material, likely improving its hardness and wear resistance (12).
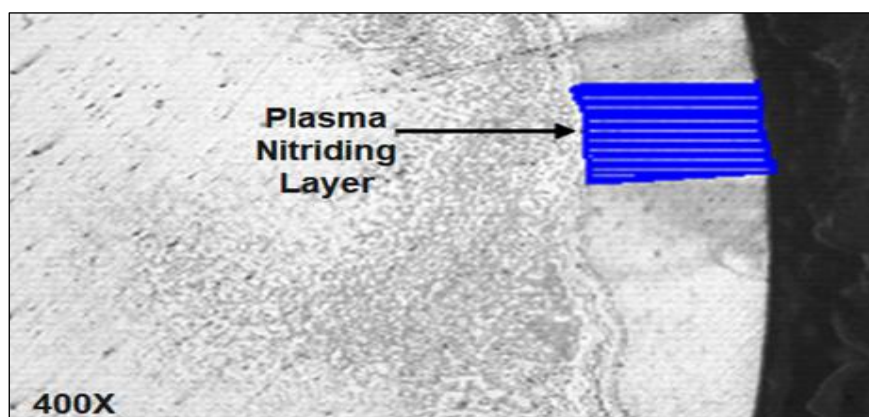
**Figure 6:** Plasma Nitriding Case Depth Layer

Tafel Plot Analysis

Corrosion behaviour (pitting corrosion) of bare and plasma nitrided SS316L conducted in the accelerated in GGBS concrete electrolyte. After 12 h plasma nitriding of SS316L specimen, case depth of nitrogen diffusion layer (CrN) is measured, i.e. 54 μm. The CrN layer and Cr_2O film have properties to reduce material corrosion rate (13). Figure 7 depicts Tafel polarization curve of bare SS316L and Plasma nitrided in a concrete mixture column. Table 3 compiles the Polarization parameters of SS316L and plasma-nitrided SS316L during the corrosion test.

Table 3: Polarization Parameters of SS316L and Plasma Nitrided SS316L during Corrosion Test

Parameters	Bare SS316L		Plasma Nitrided SS316L		Bare SS316L		Plasma Nitrided SS316L	
	Experimental				**Simulation**			
	Sample 1	**Sample 2**	**Sample 1**	**Sample 2**	**Sample 1**	**Sample 2**	**Sample 1**	**Sample 2**
Electrolyte Conductivity(S/m)	2.5	2.5	2.5	2.5	2.5	2.5	2.5	2.5
Current Density (A/cm^2)	2.4×10^{-9}	2.22×10^{-9}	0.50×10^{-9}	0.49×10^{-9}	2.12×10^{-9}	2.13×10^{-9}	0.33×10^{-9}	0.32×10^{-9}
Electrode Potential(V)	-0.240	-0.239	-0.190	-0.191	-0.277	-0.277	-0.198	-0.197
Anodic Tafel Slop (ßa) (V/dec)	0.095	0.094	0.075	0.076	0.098	0.097	0.080	0.081
Cathodic Tafel Slop (ßc) (V/dec)	0.195	0.194	0.165	0.166	0.198	0.199	0.177	0.178
Corrosion Rate(C.R.)(mpy)	0.6112	0.6121	0.01225	0.0124	0.6012	0.6011	0.01125	0.01124
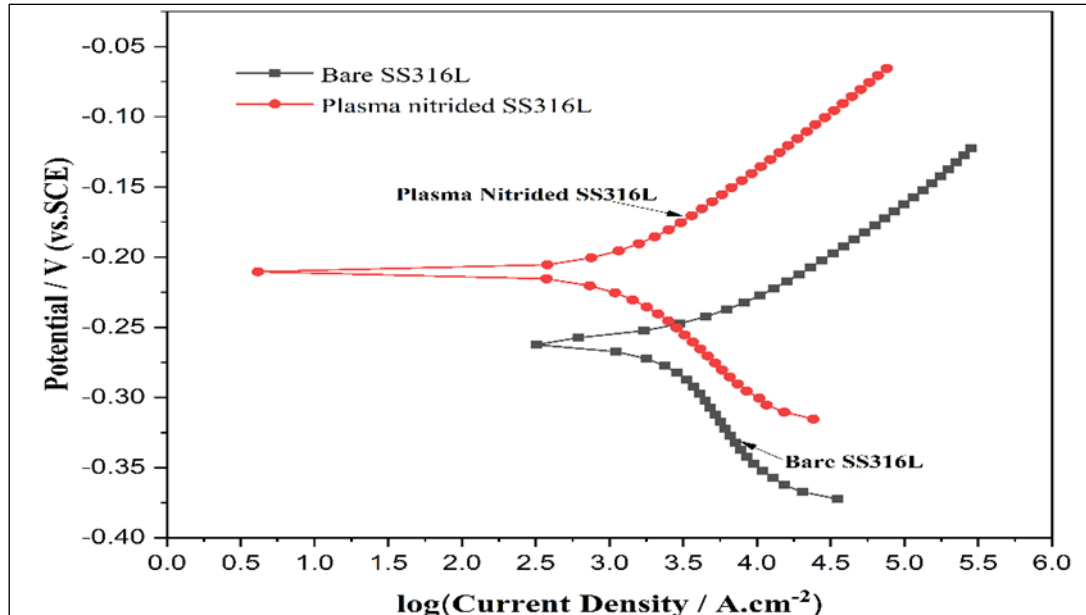
Figure 7: Tafel Polarization Curve of Bare SS316L and Plasma Nitrided in GGBS Concrete Mixture

Pitting Corrosion Analysis for SS316L and Plasma Nitrided SS316L Specimen in GGBS Concrete Environments

Two cases of bare SS316L and plasma nitrided material are considered in measurement corrosion parameters in GGBS concrete environments. Six samples are subjected to experimentation, from which three samples are bare SS316L and three samples are 12 h plasma nitrided SS316L in Concrete environments. All these tests are conducted at 1.5 mV/sec. Two case tests were conducted with repeatability for improvement of results.

Case-I: Pitting Corrosion Analysis of SS316L specimen in GGBS Concrete Environments

All surface of the 3D column model is considered electrically insulated ($\nabla n\ \phi=0$). The equations were solved, and with the help of predefined boundary conditions, the concrete's potential and i_{corr} patterns were calculated using FEM and a secondary current distribution module with time-dependent Comsol Multiphysics (14, 15). The corrosion active zone pits exhibit an estimated average pitting i_{corr} of 2.4×10^{-9} A/cm² bare SS316L material (Figure 5). In contrast, the average simulated corrosion current density (i_{corr}) is 2.1×10^{-9}A/cm² bare SS316L material (Figure 9). To illustrate elliptical pit effects on corrosion pits evolutions. At time t = 5 years, the electric potential ranges from -0.277 V(SCE) across the cathodic region over the anodic area. It should be noted that the mixed potential theory estimates the potential of the same pitting corrosion to be -0.240 V(SCE), as shown in Figure 5. Figure 9 displays the numerical outcomes for the average corrosion current density (i_{corr}) at the active pit zone in bare SS316L. According to the modelling results, an elevation in the corrosion current density (i_{corr}) is 2.12×10^{-9}A/cm², is observed when there is an increase in oxygen permeability, specifically in the scenario of pitting corrosion size at the active zone. The reason behind this pattern becomes evident when examining the oxygen concentration at the interface between steel and GGBS concrete, as depicted in Figure 5. From experimentation corrosion rate (mpy) of bare SS316L is 0.6112 mpy, and by Comsol multiphysics software corrosion rate is 0.6012 mpy.
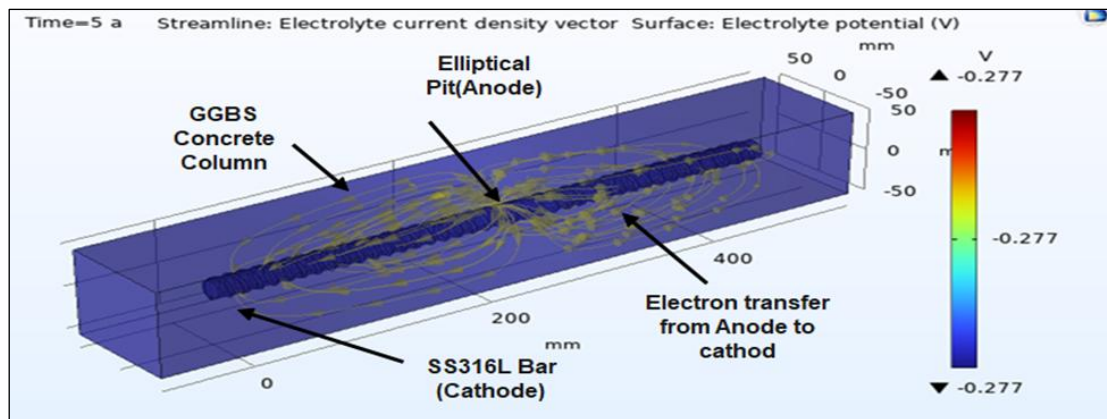
Figure 8: Electrolyte Potential (A/cm²) of bare SS316L in GGBS Concrete Environments

Figure 8 depicts the potential gradients in a concrete environment where small pits serve as active zones and the rest of the bar area remains passive. As anticipated under equilibrium conditions, in each simulation, the active pits of SS316L steel experience an anodic polarization potential of -0.277V. This demonstrates the stark contrast between the active corrosion sites and the passivized regions, which is critical for understanding localized corrosion propagation in reinforced concrete structures.
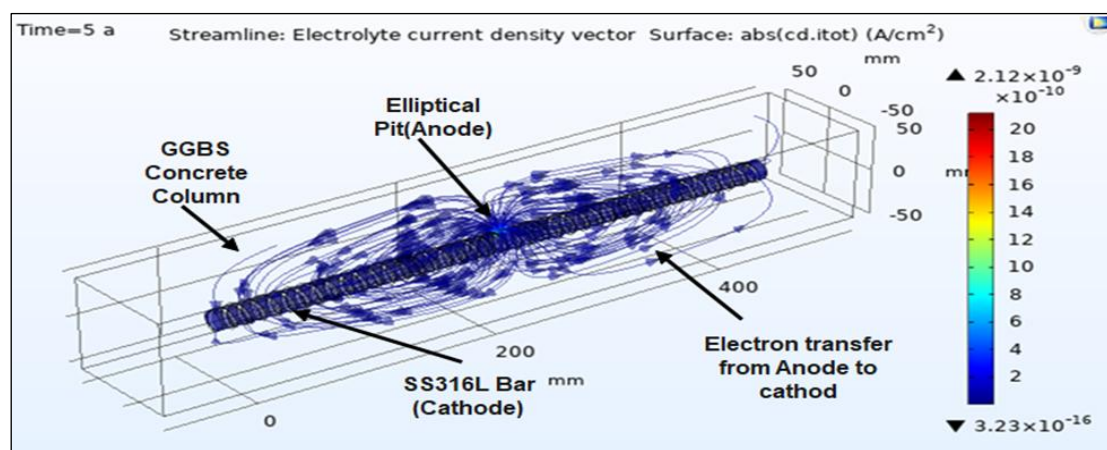

Figure 9: Current Electrolyte Density (A/cm²) of bare SS316L in GGBS Concrete Environment

Figure 9 displays the current electrolyte density streamlines in the bare SS316L simulation, with the thickness of the lines indicating the local norm of the current density vector. The figure clearly demonstrates the significant effect of resistivity, as the majority of the exchanged current flows directly from the active bar pits to the passive

areas (highlighted in red and light blue). The highest current electrolyte density, 2.12×10^{-9} A/cm^2, is observed in the small pit area. This concentration of current in small areas contributes significantly to the progression of pitting corrosion, leading to further degradation of the material.
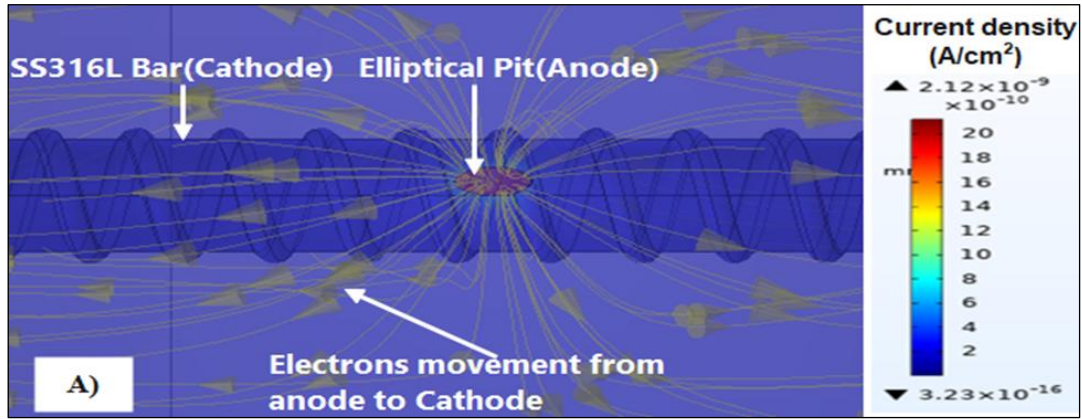
Figure 10: A) Removed Section of SS316L Concrete Rebars Elliptical Section and Streamlines of the 3D GGBS Concrete Column
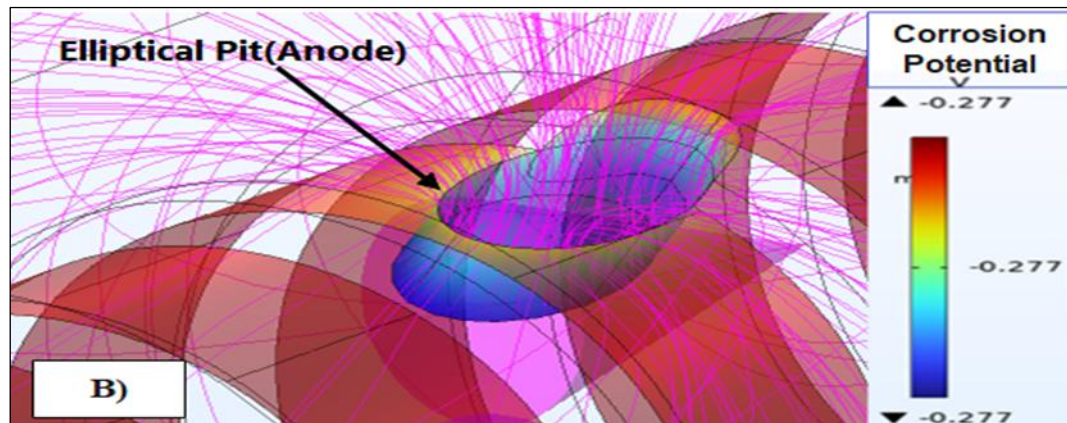
**Figure 10:** B) Removed Section of SS316L Concrete Rebars Elliptical Pit (Anode)

Figure 10 shows the removed section of SS316L concrete rebar's elliptical section and streamlines when the small pits are subjected to pitting corrosion. As the pits grow, the streamlines become more concentrated at these active zones, indicating increasing electrochemical activity and material dissolution. The elliptical shape of the pit also influences the flow of ions, potentially leading to asymmetrical growth patterns. This representation underscores the dynamic nature of pitting corrosion, where the geometry of the pit and the surrounding current flow play critical roles in determining the rate and extent of material degradation.

Case-II: Pitting Corrosion Analysis of Plasma Nitrided SS316L

The average pitting corrosion current density (i_{corr}) in the corrosion active zone pits is assessed to be $0.5 \times 10^{-9} A/cm^2$ 12 h plasma nitrided SS316L material. In contrast, the average simulated corrosion current density (i_{corr}) is determined to be 0.33×10^{-9} A/cm^2 (Figure 13) 12 h plasma nitrided SS316L. To demonstrate the effects of elliptical pits on corrosion pit evolution. At time t = 0, the electric potential in the cathodic region ranges from -0.198 V (SCE) to -0.198 V (SCE) in (Figure 12) the anodic area. As illustrated in Fig. 5, the mixed potential theory estimates the potential of the same pitting corrosion to be -0.190 V (SCE). The simulation results for the average corrosion current density (i_{corr}) 0.33×10^{-9}

A/cm^2 at the accelerated pit area in 12 h plasma nitrided SS316L are shown in Figure 12. According to the modelling results, a decrease in oxygen permeability causes a reduction in corrosion current density (icorr), specifically in pitting corrosion size at the active zone. From experimentation corrosion rate (mpy) of plasma nitrided SS316L is 0.01225 mpy, and by Comsol multiphysics software corrosion rate is 0.01125mpy in GGBS concrete environment. Due to plasma nitriding, the 54 μm diffusion layer (CrN) formed on the specimen, and the corrosion current density of the plasma nitrided specimen will decrease compared to bare SS316L material. A passive layer (Cr$_2$O) will form on the surface of plasma nitrided SS316L material. Both CrN and Cr$_2$O will impact the pitting corrosion of rebar material in GGBS concrete environments (16-20). The observed differences in corrosion behavior between bare and plasma-nitrided SS316L can be attributed to several mechanisms beyond those mentioned. One key factor is the enhanced surface hardness and reduced porosity of the plasma-nitrided layer, which provides an effective barrier against aggressive ions, such as chloride, that initiate pitting corrosion in the GGBS concrete environment. Additionally, the diffusion layer (CrN) formed during plasma nitriding increases the material's resistance to localized electrochemical reactions by reducing the number of active sites available for corrosion initiation. Another mechanism involves the refined microstructure of the plasma-nitrided layer. This microstructure promotes a more uniform distribution of stresses and minimizes crevice formation, further reducing the likelihood of pitting corrosion. Furthermore, the formation of Cr$_2$O, a stable passive oxide layer, enhances the self-repair capability of the material. This passive layer acts as a dynamic barrier, re-forming quickly if disrupted and thereby sustaining the material's corrosion resistance. Finally, the synergistic effects of CrN and Cr$_2$O layers improve the electrochemical stability of the nitrided surface, lowering its susceptibility to environmental changes such as variations in pH and oxygen availability. These combined mechanisms result in a significantly lower corrosion current density and reduced overall corrosion rate in plasma-nitrided SS316L compared to its bare counterpart in GGBS concrete environments. In sound GGBS concrete, a relatively lesser tendency for corrosion may lead to a more pronounced cathodic reaction within the accelerated pitting corrosion zone. Conversely, a relatively greater susceptibility to corrosion might yield a diminished cathodic response within the passive region. The concentration of oxygen tends to be reduced in the active zone due to greater oxygen consumption. If a pit forms in the active area, a sufficient oxygen supply could promote the local cathodic reaction, causing the oxygen concentration at the steel/concrete boundary to approach the surface-level concentration. The deterioration rate of steel was found to begin rising at a critical longitudinal crack width between 0.1 and 0.2 mm (21). Moreover, it is highlighted that longitudinal cracks could significantly elevate the microcell corrosion rate, even in High-Performance Concrete (HPC) incorporating slag or fly ash. Figures 11 and 15 depict the removed section of SS316L concrete rebars' elliptical section and streamlines of the 3D concrete column (22-25).
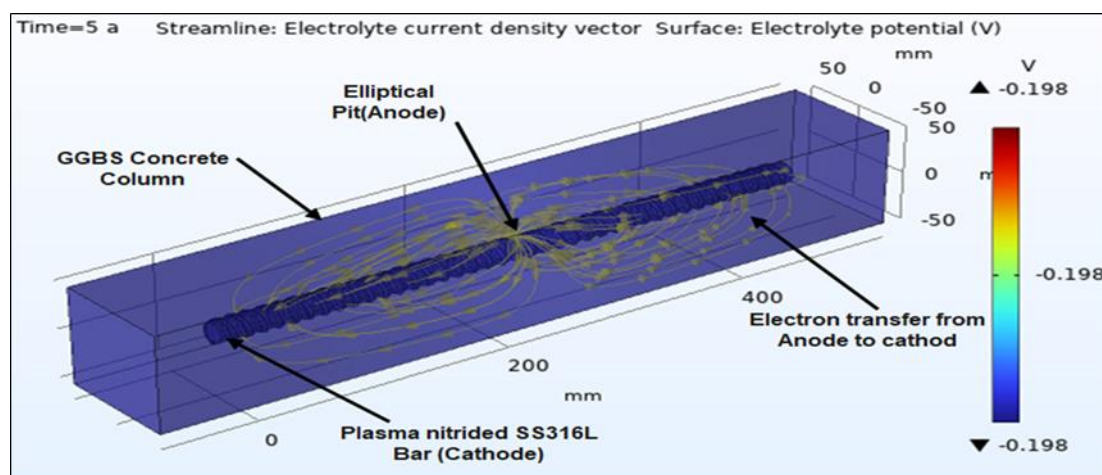
Figure 11: Electrolyte Potential (A/cm^2) of 12h Plasma Nitrided SS316L in GGBS Concrete Environment

Figure 11 shows the potential gradients achieved in the concrete environment with small pits acting as active zones and the remaining portion of the bar area acting as a passive area. Plasma nitriding enhances the corrosion resistance of SS316L in GGBS (Ground Granulated Blast Furnace Slag) concrete environments by forming a nitrogen-enriched surface layer. This layer modifies the electrochemical behavior of the steel, shifting the material into a more passive state, which helps mitigate localized corrosion. The active pits on the plasma nitrided SS316L experience anodic polarization at -0.198V, reflecting a typical corrosion potential in this aggressive environment. However, the remaining passive regions of the steel maintain a more stable potential, improving overall durability and reducing the susceptibility to corrosion in concrete structures.
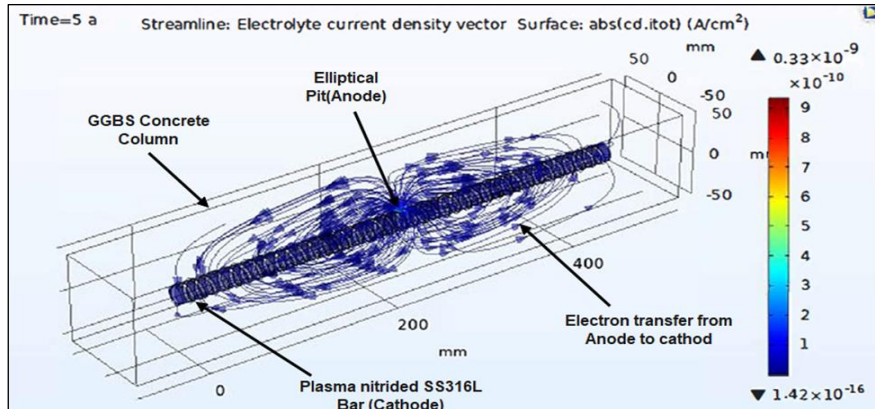

Figure 12: Current electrolyte Density (A/cm^2) of 12h Plasma Nitrided SS316L in GGBS Concrete Environment

Figure 12 shows current electrolyte density streamlines achieved in the case of plasma nitrided SS316L simulation thickness of lines highlighting the local norm of the current density vector. In Figure 12, the effect of the non-negligible resistivity is well illustrated by the fact that most of the exchanged current is flowing straightly from the active bar pits to the passive area (red and light blue areas). The maximum current electrolyte density of 0.33 x 10^{-9} A/cm^2 is observed at small pit area. The plasma nitriding treatment on SS316L significantly alters the electrochemical behavior within the GGBS environment, as seen in the current density streamlines in Figure 12. The treatment creates a distinct difference between the active and passive areas, with most of the current flowing from the localized pits (the active regions) to the surrounding passive areas, as indicated by the red and light blue regions. The maximum current density observed at the small pit area (0.33 x 10^{-9} A/cm^2) reflects the intensified electrochemical activity at these pits. This localized increase in current density further emphasizes the protective role of the nitrided layer, as it reduces corrosion propagation by isolating the more reactive areas.
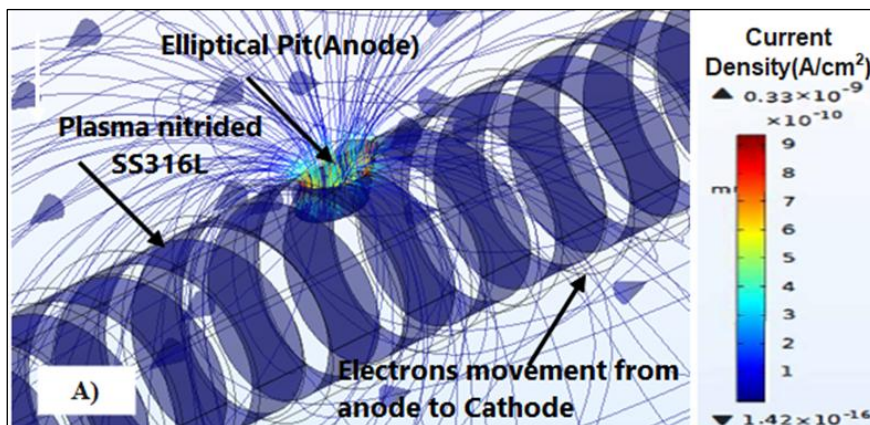
Figure 13: A) Removed Section of SS 316L Concrete Rebars Elliptical Section and Streamlines of the 3D GGBS Concrete Column
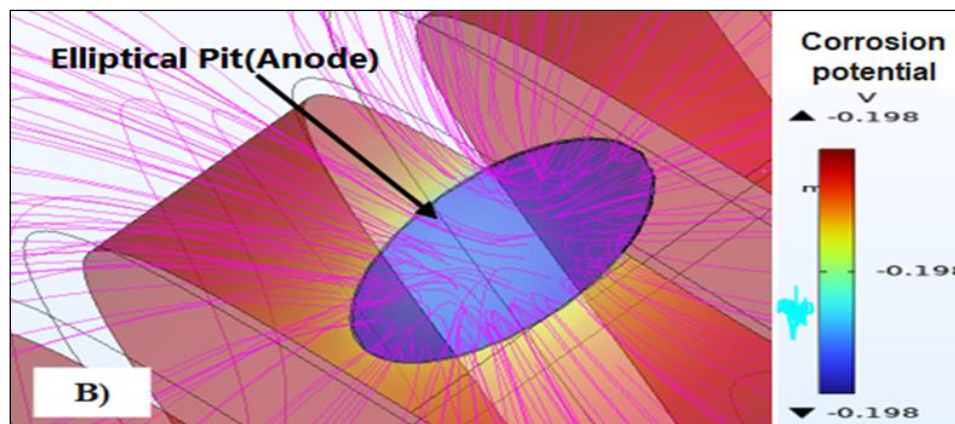
Figure 13: B) Removed Section of SS316L Concrete Rebars Elliptical Pit (Anode)

Figure 13(A) illustrates an elliptical pit on the plasma-nitrided SS316L surface, which forms due to material damage but is smaller in size compared to the pit observed on bare SS316L. The blue arrow indicates the direction of electron movement, flowing from the anode to the cathode. The plasma nitriding treatment on SS316L significantly modifies its electrochemical behavior in the GGBS environment, as evident from the current density streamlines in the figure, which establish a clear distinction between active regions, where localized pits form, and passive areas, with most current flowing from the red (active) to the light blue (passive) regions. Figure 13(B) shows a removed section of SS316L concrete rebars with an elliptical pit, which represents the anode region. The active pits on the plasma-nitrided SS316L experience anodic polarization at -0.198V, indicating a typical corrosion potential in this aggressive environment. However, the remaining passive regions of the steel maintain a more stable potential, improving overall durability and reducing the susceptibility to corrosion in concrete structures. The red color indicates higher potential towards the anodic side, while the blue color indicates the cathodic regions.

Electrochemical Impedance Analysis

The Nyquist plots in Figures 14 show the variation in impedance as a function of the real and imaginary components (Z_{re} versus Z_{im}) both before and after plasma nitriding. Figures 14 and 15 show the impedance of SS316L material with 3.5 wt% in NaCl, it shows that if the plasma nitriding process is done on the metal specimen, the impedance (i.e resistance) of metal will increase as compared to bare SS316L (26-30).
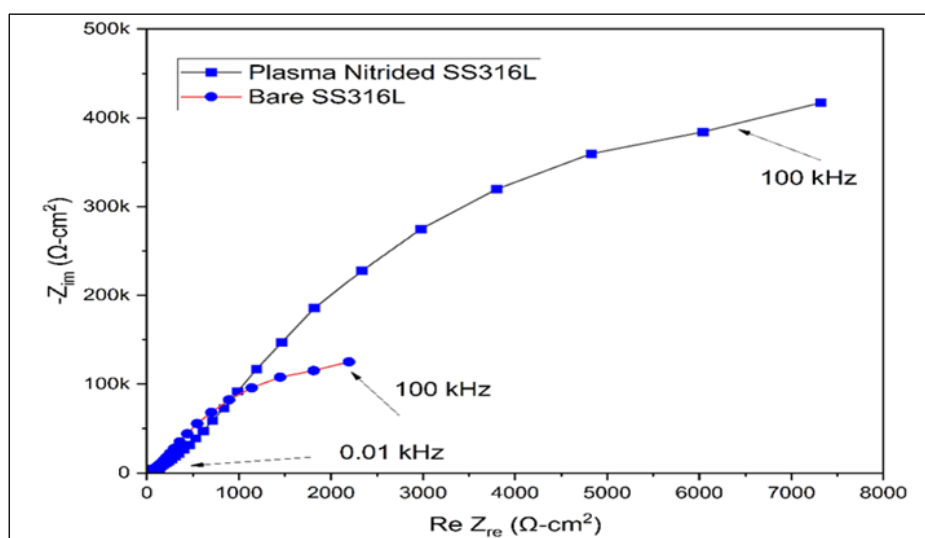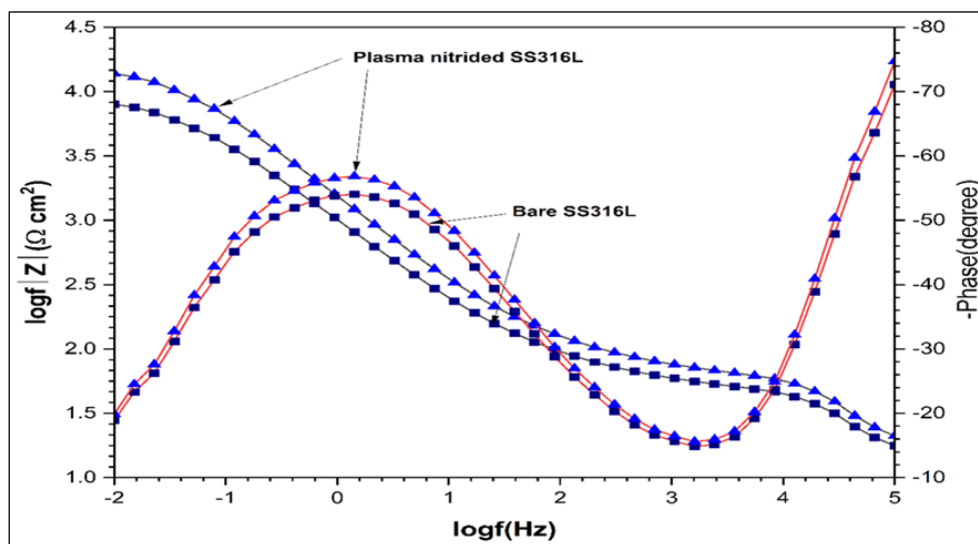

Figure 14: Nyquist Plot for Bare SS316L and Plasma Nitrided SS316L

Figure 14 compares the impedance of Plasma Nitrided SS316L and Bare SS316L stainless steel. The Plasma Nitrided SS316L shows higher impedance at lower frequencies compared to the Bare SS316L. The shape of the curves indicates the nature of the electrochemical processes and

resistance to corrosion. Plasma-nitrided SS316L exhibits a larger semicircle, implying higher corrosion resistance and better protective properties than Bare SS316L. Plasma nitriding creates a hard nitride layer on the surface of SS316L. This layer acts as a barrier to corrosive species, reducing the rate of electrochemical reactions at the surface. The nitride layer increases the overall resistance to corrosion. The nitride layer formed during plasma nitriding can slow down the diffusion of ions through the surface layer. This reduced ion mobility further contributes to the higher impedance observed in the nitrided material (31-33).


Figure 15: Bode Plot for Bare SS316L and Plasma Nitrided SS316L in GGBS Concrete Environments

Table 4: Equivalent Circuit Parameters of For Bare SS316L and Plasma Nitrided SS316L in 3.5 wt. % NaCl Solution (GGBS Concrete Environments)

Specimen	R_s (Ω-cm^2)	CPE-Y_0(Ω^{-1} cm^{-2}S^n)	N	R_p (Ω-cm^2)	W (Ω-cm^2 s$^{-0.5}$)
Bare SS316L	34.41	3.0325E^{-6}	0.69	2.0411 E^8	2.719E^{-2}
Plasma nitrided SS316L(12h)	36.40	4.5158E^{-5}	0.78	4.2158 E^5	5.171E^{-5}

The Bode plot typically shows the impedance magnitude and phase angle as a function of frequency in Figure 15. At high frequencies, both Plasma Nitrided SS316L and Bare SS316L show lower impedance magnitudes, but Plasma Nitrided SS316L consistently shows higher values. At low frequencies, the impedance magnitude for Plasma Nitrided SS316L is significantly higher, indicating better barrier properties and higher corrosion resistance. Figure 16 and Figure 17 shows electrochemical impedance circuit is simulated by using IVIUM electrochemical software. Table 4 presents the equivalent circuit parameters for bare SS316L and plasma-nitrided SS316L in a 3.5 wt. % NaCl solution, simulating GGBS concrete environments. These parameters provide insights into the electrochemical behavior, including corrosion resistance and surface properties, of the materials under these conditions. The nitrided layer enhances the formation of a passive oxide layer that is more stable and uniform, which contributes to higher impedance by reducing the corrosion rate and preventing charge transfer (34-37). Figure 18 shows the electrochemical interface between SS316L and 3.5 wt. % NaCl solutions. The phase angle differences also suggest variations in the electrochemical processes occurring on the surfaces of Plasma Nitrided SS316L and Bare SS316L. The more negative phase angle for Plasma Nitrided SS316L indicates a more capacitive behaviour, which is typical for materials with better protective layers (38-43). Overall, the higher impedance of Plasma Nitrided SS316L across the frequency spectrum in the Bode plot reaffirms the conclusions drawn from the Nyquist plot, emphasizing the enhanced corrosion resistance and electrochemical stability provided by the plasma nitriding process (44, 45).
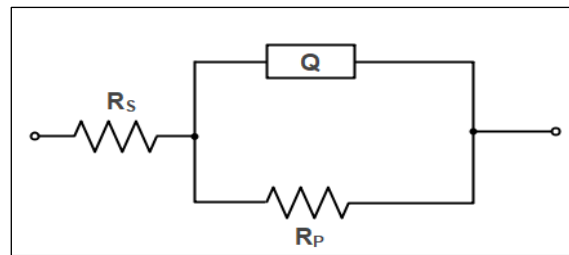
Figure 16: Electrochemical Impedance Circuit (Randle Circuit) for SS316L in 3.5 wt. % NaCl Solution
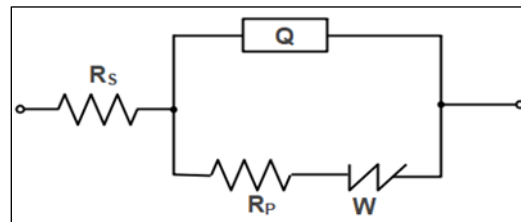
Figure 17: Electrochemical Impedance Circuit for Plasma Nitrided SS316L in 3.5 wt. % NaCl Solution
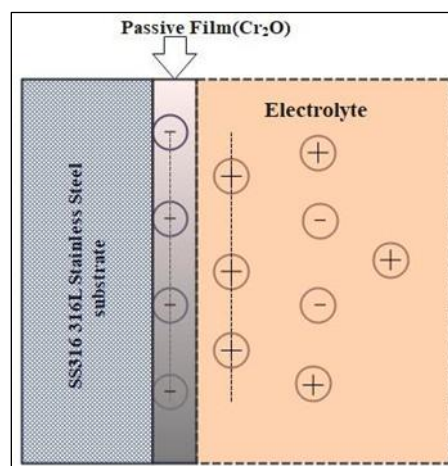
Figure 18: SS316L and 3.5 wt. % NaCl Solution Interface (GGBS Concrete Environment)

Conclusion

The investigation demonstrates that incorporating plasma nitriding specimens significantly reduces the pitting corrosion rate of SS316L in a GGBS concrete environment. The formation of the Cr_2O_3 and CrN layer contributes to a notable reduction in corrosion current density (A/cm^2) of SS316L after surface modification. Experimental results show a reduction in electrolyte potential up to -0.277V and a current density decrease to 2.4×10^{-9} A/cm^2, compared to the simulation results of bare SS316L which show a current density of up to 2.42×10^{-9} A/cm^2. The corrosion rate of bare SS316L is observed experimentally as 0.6112 mpy, and by simulation software as 0.6012 mpy. For plasma nitrided SS316L, experimental results indicate an electrolyte potential of up to -0.190V, while tafel polarization results from simulation software show an electrolyte potential of -0.198V

for 12-hour plasma nitrided specimens. Potentiodynamic tests reveal a current density of up to 0.50×10^{-9} A/cm^2 for 12-hour plasma nitrided specimens in a GGBS concrete environment. Simulation results from Comsol multiphysics simulate a current density of 0.33×10^{-9} A/cm^2 for plasma nitrided SS316L in a concrete environment. The corrosion rate of bare SS316L is observed experimentally as 0.01225 mpy and by simulation software as 0.01125 mpy. These results suggest that plasma nitriding surface modification increases the corrosion resistance of SS316L, resulting in a significant improvement in the lifespan of in GGBS concrete rebar, potentially extending it by 50 times. Specifically, the corrosion current density decreases by approximately 80% and the electrolyte potential increases by around 31%. Overall, the study highlights that plasma nitriding surface modification can significantly enhance the durability of GGBS concrete structures.

Abbreviation

Nil.

Authors Contributions

Dr. Amol Mali, Dr. Aniket Kolekar, Dr. Vikas Dive, Dr. Sandesh Solepatil, Dr. Ganesh Jadhav,and Dr. Sashikant Vagge played an equal role in the research and writing of this manuscript. Dr.Amol Mali and Dr. Aniket Kolekar was responsible for conceptualizing the research concept, devising and executing the experiments, evaluating the data, and composing the manuscript.

Conflict of Interest

The authors declare no conflict of interest.

Ethics Approval

Not applicable.

References

1. Laycock NJ, White SP. Computer simulation of single pit propagation in stainless steel under potentiostatic control. J Electrochem Soc. 2001;148(7): 65-71.
2. Ahmad S. Reinforcement corrosion in concrete structures, its monitoring and service life prediction–a review. Cement Concr Compos. 2003;25(4–5):459–471.
3. Vidal A, Castel A, François R. Analyzing crack width to predict corrosion in reinforced concrete. Cement Concr Res. 2004;34(1):165–174.
4. Warkus J, Raupach M. Modeling of reinforcement corrosion–Corrosion with extensive cathodes. Mater Corros. 2006;57(12):920–925.
5. Almusallam AA, Al-Gahtani AS, Aziz AR. Effect of reinforcement corrosion on bond strength. Constr Build Mater. 1996;10(2):123–129.
6. Pease B, Geiker M, Stang H, Weiss J. The design of an instrumented rebar for assessment of corrosion in cracked reinforced concrete. Mater Struct. 2011;44:1259–1271.
7. Xiao J, Chaudhuri S. Predictive modelling of localized corrosion: An application to aluminium alloys. Electrochim Acta. 2011;56(16):5630–5641.
8. Wang H, Han EH. Computational simulation of corrosion pit interactions under mechanochemical effects using a cellular automaton/finite element model. Corrosion Science. 2016;103:305-311.
9. Kenny A, Katz A. Steel-concrete interface influence on chloride threshold for corrosion–Empirical reinforcement to theory. Constr Build Mater. 2020;244:118-126.
10. IS 1727. Methods of test for pozzolanic materials. New Delhi, India: Bureau of Indian Standards; 1967.https://law.resource.org/pub/in/bis/S03/is.1727.1967.pdf
11. Vu TH, Dang LC, Kang G, Sirivivatnanon V. Chloride induced corrosion of steel reinforcement in alkali activated slag concretes: A critical review. Case Stud Constr Mater. 2022;16(3):1-13.
12. Arya C, Vassie PRW. Influence of cathode-to-anode area ratio and separation distance on galvanic corrosion currents of steel in concrete containing chlorides. Cement Concr Res. 1995;25(5):989–998.
13. Zhang X, Zheng S, Zhao X. Experimental and numerical study on seismic performance of corroded steel frames in chloride environment. J Constr Steel Res. 2020;171:106164:1-15.
14. Jasper S, Vijayakumar D, Stalin B, Rajesh S, Jhansi Ida S. Experimental investigation of a multilayer nitride coating deposited on austenitic coating steel. Mater Today Proc. 2023;74(1):117–121.
15. Cai Y, Zhang W, Yu L, Chen M, Yang C, François R, Yang K. Characteristics of the steel-concrete interface and their effect on the corrosion of steel bars in concrete. Constr Build Mater. 2020;253:1–13.
16. Li S, Lv H, Huang T, Zhang Z, Yao J, Ni X. Degradation of reinforced concrete beams subjected to sustained loading and multi-environmental factors. Buildings. 2022;12(9):138-152.
17. Kumar TU, Kumar MV. Study on corrosion-induced R.C. beams using slag-based geopolymer aggregate concrete. Mater Today Proc. 2023;14:122–130.
18. Macdonald DD. The point defect model for the passive state. J Electrochem Soc. 1992;139(12):3434.
19. Borgioli F, Fossati A, Galvanetto E, Bacci T. Glow-discharge nitriding of AISI 316L austenitic stainless steel: Influence of treatment temperature. Surf Coat Technol. 2005;200(7):2474–2480.
20. Cavalier PG, Vassie PR, TRRL. Investigation and repair of reinforcement corrosion in a bridge deck. Proc Inst Civ Eng. 1981;70(3):461–480.
21. Yuan Y, Jiang J, Peng T. Corrosion process of steel bar in concrete in full lifetime. ACI Mater J. 2010;107:562–567.
22. Michel A, Otieno M, Stang H, Geiker MR. Propagation of steel corrosion in concrete: Experimental and numerical investigations. Cement Concr Compos. 2016;70:171–182.
23. Chen L, Leung RS, Su R. On the corrosion rate measurement of reinforcing steel in chloride induced macrocell corrosion. Cement Concr Compos. 2022;134:1047-1075.
24. Singh A, Thirumurugesan R, Krishnakumar S, Rani R, Chandramouli S, Parameswaran P, Mythili R.

Performance evaluation of plasma nitrided 316L stainless steel during long term high-temperature sodium exposure. Nucl Eng Technol. 2023;55(4):1468–1475.

25. Venkatesan SP, Jeevahan J, Purusothaman M, Venkatesh S, Rakesh Vimal M. Corrosion and mechanical behaviour of plasma nitrated metallic biomaterial surfaces. Mater Today Proc. 2021;47(4):938–943.

26. Asgari M, Barnoush A, Johnsen R, Hoel R. Microstructural characterization of pulsed plasma nitrided 316L stainless steel. Mater Sci Eng A. 2011;529:425–434.

27. Kartikasari R, Sutrisna. Corrosion behavior of plasma nitrided SS316L biomaterial. The Open Mater Sci J. 2017;11:29–37.

28. IS 10262. Guidelines for concrete mix design proportioning. New Delhi, India: Bureau of Indian Standards; 2009. https://law.resource.org/pub/in/bis/S03/is.10262.2009.pdf

29. Kear G, Barker BD, Stokes KR, Walsh FC. Corrosion and impressed current cathodic protection of copper-based materials using a bimetallic rotating cylinder electrode (BRCE). Corros Sci. 2005;47(7):1694–1705.

30. Elsener B. Corrosion of steel in concrete. Corros Environ Degrad. 2000;2:389–436.

31. Chauhan A, Desai YM, Banerjee S, Sharma UK. 3D simulation of non-uniform corrosion-induced damage in reinforced concrete exposed to real climate. Struct. 2023;56:104-122.

32. Tian Y, Zhang G, Ye H, Zeng Q, Zhang Z, Tian Z, Jin X, Jin N, Chen Z, Wang J. Corrosion of steel rebar in concrete induced by chloride ions under natural environments. Constr Build Mater. 2023;369:130-144.

33. Williamson J, Isgor OB. The effect of simulated concrete pore solution composition and chlorides on the electronic properties of passive films on carbon steel rebar. Corros Sci. 2016;106:82–95.

34. Singh JK, Singh DDN. The nature of rusts and corrosion characteristics of low alloy and plain carbon steels in three kinds of concrete pore solution with salinity and different pH. Corros Sci. 2012;56:129–142.

35. Tawfik TA, El-Yamani MA, Abd El-Aleem S, Serag Gabr A, Abd El-Hafez GM. Effect of nano-silica and nanowaste material on durability and corrosion rate of steel reinforcement embedded in high-performance concrete. Asian J Civil Eng. 2019;20:135–147.

36. Revert AB, De Weerdt K, Hornbostel K, Geiker MR. Carbonation-induced corrosion: Investigation of the corrosion onset. Constr Build Mater. 2018;162:847-856.

37. Cao C, Cheung MMS, Chan BYB. Modelling of interaction between corrosion-induced concrete cover crack and steel corrosion rate. Corros Sci. 2013;69:97-109.

38. Zhu X, Zi G. A 2D mechano-chemical model for the simulation of reinforcement corrosion and concrete damage. Constr Build Mater. 2017;137:330-344.

39. Ye Z, Zhang W, Gu X. Deterioration of shear behaviour of corroded reinforced concrete beams. Eng Struct. 2018;168:708-720.

40. Wang H, Jiang M, Hang M, Yang Y, Zhou X, Liu X, Xu G. Inhibition resistance and mechanism of migrating corrosion inhibitor on reinforced concrete under coupled carbonation and chloride attack. J Build Eng. 2023;76:107398.

41. Fang X, Pan Z, Ma R, Chen A. A multi-phase-field framework for non-uniform corrosion and corrosion-induced concrete cracking. Comput Methods Appl Mech Eng. 2023;414:116-196.

42. Du X, Jin L, Zhang R. Modeling the cracking of cover concrete due to non-uniform corrosion of reinforcement. Corros Sci. 2014;89:189-202.

43. Robino CV, Inal OT. Ion nitriding behaviour of several low alloy steels. Mater Sci Eng. 1983;59:79-90.

44. Dalibon EL, Moscatelli M, Simison S, Escalada L, Cabo A, Lasorsa C, Brühl SP. Corrosion behaviour of a SiOxNy coated and nitrided P.H. stainless steel. Procedia Mater Sci. 2015;8:29-38.

45. Hamedpour F, Mohseni E, Yazdi MA. Effect of plasma nitriding on corrosion resistance of 316L stainless steel in chloride environments. Surf Coat Technol. 2018;344:565-573.